Ocean Systems Engineering, *Vol. 15, No. 2 (2025) 195-217*
https://doi.org/10.12989/ose.2025.15.2.195

Numerical solution of ocean wave propagation using integrated σ-transformation and finite difference methods

Nasim Madah Shariati*

Department of Applied Mathematics, Faculty of Mathematical Sciences, University of Guilan, Namjoo Street, Rasht, 41938-33697, Iran

(Received March 27, 2025, Revised June 10, 2025, Accepted June 15, 2025)

Abstract. This paper provides a novel numerical approach in order to simulate ocean wave propagation, integrating σ-transformation with the finite difference schemes. The governing equations are derived from viscous flow theory, specifically the incompressible Navier-Stokes equations under the assumption of negligible viscosity (Euler's equations). The continuity equation represents the conservation of mass and is a fundamental part of fluid dynamics, applicable to both potential flow theory and viscous flow theory, and momentum equations represent the conservation of momentum in the horizontal and vertical directions, respectively. The method enhances accuracy and stability in modeling wave dynamics in deep and transitional waters while effectively handling complex geometries and boundary conditions. Numerical experiments indicate high precision and the capability to capture nonlinear wave behavior, particularly in comparisons with linear and second-order Stokes theory. Stability analyses confirm that the framework maintains reliable results across varying time steps with minimal error growth. This research provides a powerful tool for ocean wave simulation, holding significant implications for marine engineering, environmental studies, and coastal management.

Keywords: finite difference method; numerical solution; numerical stability and accuracy; ocean wave propagation; σ-transformation

1. Introduction

With ongoing advancements in computational technologies, numerical modeling has established itself as a fundamental tool for analyzing and understanding complex marine phenomena (Khater 2023, Zheng and Zhang 2024, Shirkavand and Farrahi-Moghaddam 2024). Numerical methods provide a framework for solving partial differential equations that govern a wide range of marine processes, including wave dynamics (Kurt *et al*. 2020). Among the most widely used techniques are the finite difference (FD) method, which approximates solutions over structured grids; the finite element (FE) method, which divides irregular domains into smaller, manageable elements; and the finite volume (FV) method, which integrates conservation laws over discrete control volumes. Each method is uniquely suited to particular challenges, contributing to the versatility and effectiveness of numerical approaches in marine studies.

The FD method, in particular, has been extensively employed in various applications.

*Corresponding author, Dr., E-mail: madah_nasim98@phd.guilan.ac.ir

http://www.techno-press.org/?journal=ose&subpage=7 ISSN: 2093-6702 (Print), 2093-677X (Online)

Maâtoug and Ayadi (2016) utilized the Crank–Nicholson approach combined with the FD method to model second-order Stokes theory, enabling accurate predictions of potential flow and surface elevation. Lundgren and Mattsson (2020) introduced a high-order explicit upwind FD scheme for solving shallow water equations with enhanced stability. Xu *et al*. (2021) advanced FD techniques by incorporating an immersed boundary method to address nonlinear wave dynamics in domains with free surface conditions and complex seabed geometries. Similarly, Qi *et al*. (2024) developed a 3D linear frequency domain FD framework to predict wave behavior in shallow basins under external forces. Additionally, Wang and Liu (2011) proposed a modified leap-frog FD scheme optimized for nonlinear shallow water equations, enhancing efficiency and accuracy.

The FV method has also seen significant developments. For instance, Benkhaldoun and Seaïd (2010) proposed a novel FV approach for solving shallow water equations, enabling simulations of water behavior over varying surface features. Similarly, the FE method has proven effective for modeling complex wave dynamics in domains with irregular geometries and variable bathymetry. Notable examples include the random FE approach (Zhu *et al*. 2022), unstructured FE models (Agarwal *et al*. 2022), hybrid FE methods (Kumar 2018), and depth-integrated non-hydrostatic FE models (Wei and Jia 2014). To further improve computational efficiency and accuracy, domain transformation techniques have gained attention. Among them, the σ-transform has emerged as a powerful method for mapping complex physical domains into simpler computational ones, facilitating the application of numerical methods to challenging problems (Lin and Li 2002, Turnbull *et al*. 2003). The σ-transform, when integrated with advanced numerical techniques, has demonstrated remarkable potential in fluid mechanics and wave dynamics. For instance, Yang *et al*. (2024) introduced a σ-transform-based FE method to simulate fully nonlinear potential flows, while Klahn *et al*. (2020) developed a σ-transform-based Fourier-Legendre-Galerkin model to analyze nonlinear water wave phenomena.

While sigma-coordinate transformations and finite-difference methods have long been employed in marine modeling, their combined application to wave equations remains scarce and, to date, has been confined to free-surface formulations (Lin and Li 2002, Turnbull *et al*. 2003). No studies to date have coupled a sigma-transform with a multi-layer finite-difference discretization, and existing single-layer approaches frequently may exhibit numerical smoothing and instability in the near-bed region. Here, a novel multi-layer finite-difference scheme in sigma coordinates is introduced that solves the full set of wave equations throughout the water column, thereby capturing depth-varying dynamics absent in earlier models. The method preserves vertical structure and numerical stability in all layers, resolves wave kinematics not only at the free surface but at each depth level, and employs an explicit two-stage predictor–corrector algorithm that attains second-order temporal accuracy for the sigma-transformed momentum equations. Validation against analytic wave profiles demonstrates that the approach achieves desirable accuracy.

It is also important to note that, in addition to these traditional methods, meshless methods have also gained increasing attention in the field of computational fluid dynamics. In particular, the smoothed particle hydrodynamics (SPH) method has proven to be especially effective in modeling complex marine and coastal processes, including free surface flows, wave breaking, and wave-structure interactions (Monaghan 1994, Liu and Liu 2010, Ghoneim 2025).

The structure of this paper is as follows: Section 2 introduces the governing equations along with the associated boundary and initial conditions. Section 3 outlines a domain mapping technique that transforms irregular physical domains into regular computational ones suitable for numerical calculations. Under this transformation, practical numerical schemes based on FD

methods are developed, and a numerical algorithm is formulated to solve the equations. Section 4 presents the application of the proposed method, showcasing the results, error graphs, and an assessment of its accuracy, consistency and stability. Finally, Section 5 discusses the findings in detail. Proofs of the numerical scheme's consistency are provided in Appendix A.

2. Mathematical modeling of ocean waves

2.1 Governing equations

The modeling of ocean waves involves deriving the fundamental equations governing the wave dynamics using boundary conditions defined at the free surface and seabed within a two-dimensional domain. The conservation of mass is represented by the continuity equation (Bakhoday 2015, Paskyabi 2016, Bakhoday 2017, Ning *et al*. 2023)

$$\frac{\partial u}{\partial x}+\frac{\partial w}{\partial z}=0 \tag{1}$$

In this equation, u is the horizontal velocity in the x-direction, and w is the vertical velocity in the z-direction. The variables x and z represent the horizontal distance along the water's surface and the depth in the water column, respectively. The momentum equations, which govern the wave motion in both the horizontal and vertical directions, are as follows

$$\frac{\partial u}{\partial t}+u\frac{\partial u}{\partial x}+w\frac{\partial u}{\partial z}=-\frac{1}{\rho}\frac{\partial p}{\partial x} \tag{2}$$

$$\frac{\partial w}{\partial t}+u\frac{\partial w}{\partial x}+w\frac{\partial w}{\partial z}=-\frac{1}{\rho}\frac{\partial p}{\partial z} \tag{3}$$

Here, t represents time, ρ is the water density, and p denotes the pressure. The dynamic pressure equation at the wave surface, incorporating the effects of gravity and surface wave interactions, is given by

$$\left.\frac{\partial p}{\partial t}\right|_{z=0}=-\rho g\frac{\partial}{\partial x}\int_{-d}^{\eta}u dz \tag{4}$$

In this equation, $z=0$ corresponds to the wave surface and d represents the seabed depth. $\eta(x,t)$ is the wave surface profile. To simplify the analysis, especially for linear wave theory, the nonlinear terms in the momentum equations are neglected, resulting in the following linearized equations for velocity components

$$\frac{\partial u}{\partial t}=-\frac{1}{\rho}\frac{\partial p}{\partial x} \tag{5}$$

$$\frac{\partial w}{\partial t}=-\frac{1}{\rho}\frac{\partial p}{\partial z} \tag{6}$$

2.2 Boundary conditions

The boundary conditions for this model are outlined below:

- Wave Surface Conditions: The conditions at the free surface are defined as:

$$\frac{\partial u}{\partial z} = 0, \frac{\partial w}{\partial z} = 0, p = \rho g \eta$$

- Boundary Conditions at the Sides: Periodic boundary conditions are assumed on both the left and right boundaries of the domain.
- Seabed Conditions: The conditions at the seabed are given by:

$$\frac{\partial u}{\partial z} = 0, w = 0, \frac{\partial p}{\partial z} = 0$$

Boundary conditions declare that at the free surface, vertical variations of horizontal and vertical velocity of water particles are not evident, suggesting that pressure variations have a negligible effect on these variations at the surface. On the other hand, top close layers have the same behavior. At the bottom boundary, both vertical variations of horizontal velocity and pressure are minimal, aligning with the assumption of an impermeable and rigid seabed. These conditions are consistent with the understanding that pressure gradients can induce variations in particle velocities within the fluid body, especially when external forces or conditions introduce non-uniformities.

2.3 Initial conditions

The initial conditions for wave elevation, velocities, and pressure under linear wave theory are presented in Eq. (7). The constant c is given by Eq. (8). For a more precise representation of wave dynamics, particularly in cases involving nonlinear effects, the second-order Stokes wave theory introduces higher-order corrections to the wave elevation, particle velocities, and pressure. These corrections are captured in Eq. (9).

$$\begin{aligned}
&\eta(t,x)\big|_{t=0} = a\sin(\omega t - kx)\big|_{t=0} \\
&u(t,x,z)\big|_{t=0} = [ck\cosh[k(z+d)]\sin(\omega t - kx)]\big|_{t=0} \\
&w(t,x,z)\big|_{t=0} = [ck\sinh[k(z+d)]\cos(\omega t - kx)]\big|_{t=0} \\
&p(t,x,z)\big|_{t=0} = [\rho c\omega\cosh[k(z+d)]\sin(\omega t - kx) - \frac{\rho}{2}[ck\cosh[k(z+d)]\sin(\omega t - kx)]^2 \\
&\qquad - \frac{\rho}{2}[ck\sinh[k(z+d)]\cos(\omega t - kx)]^2\Big|_{t=0}
\end{aligned} \tag{7}$$

such that

$$c = \frac{ga}{\omega\, cosh(kd)} \tag{8}$$

$$\begin{aligned}
&\eta(t,x)\big|_{t=0} = a\sin(\omega t - kx) + \frac{\pi a^2}{2\lambda}\frac{\cosh(kd)}{\sinh^3(kd)}[2+\cosh(2kd)\cos(2(kx-\omega t))\Big|_{t=0} \\
&u(t,x,z)\big|_{t=0} = \frac{2\pi a}{T}\frac{\cosh(k(z+d))}{\sinh(kd)}\cos(kx-\omega t) + \frac{3}{4}\frac{2\pi a}{\lambda}\frac{2\pi a}{T}\frac{\cosh(2k(z+d))}{\sinh^4(kd)}\cos(2(kx-\omega t))\Big|_{t=0} \\
&w(t,x,z)\big|_{t=0} = \frac{2\pi a}{T}\frac{\sinh(k(z+d))}{\sinh(kd)}\sin(kx-\omega t) + \frac{3}{4}\frac{2\pi a}{\lambda}\frac{2\pi a}{T}\frac{\sinh(2k(z+d))}{\sinh^4(kd)}\sin(2(kx-\omega t))\Big|_{t=0} \\
&p(t,x,z)\big|_{t=0} = \rho g a\frac{\cosh(k(z+d))}{\cosh(kd)}\cos(kx-\omega t) \\
&\qquad + \frac{3}{4}\rho g\frac{4\pi a^2}{\lambda}\frac{1}{\sinh(2kd)}\times\left[\frac{\cosh(2k(z+d))}{\sinh^2(kd)} - \frac{1}{3}\right]\cos(2(kx-\omega t)) \\
&\qquad - \frac{1}{4}\rho g\frac{4\pi a^2}{\lambda}\frac{1}{\sinh(2kd)}\times[\cosh(2k(z+d))-1]\Big|_{t=0}
\end{aligned} \tag{9}$$

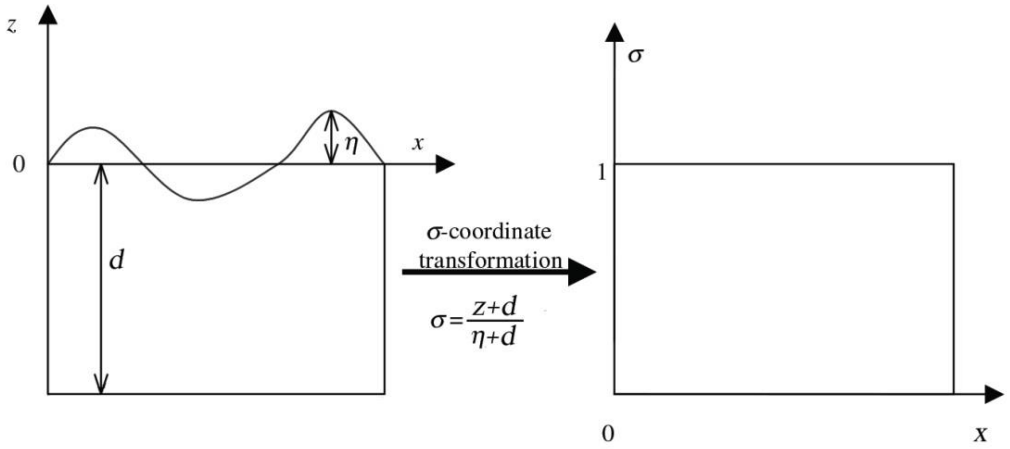

Fig. 1 Physical and computational domain

3. Computational algorithm

This section outlines a computational algorithm for simulating wave propagation in oceans, emphasizing accuracy, stability, and consistency. The FD scheme ensures precise modeling of water particle interactions across depths while minimizing numerical errors. A coordinate transformation maps the irregular physical domain into a structured computational domain, simplifying boundary conditions and improving efficiency. The algorithm effectively calculates velocity, pressure, and wave surface evolution, addressing the nonlinear dynamics of ocean waves. This robust framework provides a reliable tool for simulating complex wave phenomena in marine environments.

Due to the complexity of the nonlinear and irregular framework of the ocean, a coordinate conversion is declared and used in order to convert the physical irregular domain with (x, z, t) components to the computational regular domain with (X, σ, T) components. The following mapping is considered (Lin and Li 2002, Turnbull *et al*. 2003)

$$X = x, \sigma = \frac{z+d}{\eta+d}, h := \eta + d, T = t$$

such that $-d \le z \le \eta$ and hence $0 \le \sigma \le 1$, Fig. 1.

By using the chain rule, the derivatives can be concluded

$$\frac{\partial}{\partial x} = \frac{\partial}{\partial X} + \frac{\partial}{\partial \sigma}\frac{\partial \sigma}{\partial x}, \frac{\partial}{\partial z} = \frac{1}{h}\frac{\partial}{\partial \sigma}, \frac{\partial}{\partial t} = \frac{\partial}{\partial T} + \frac{\partial}{\partial \sigma}\frac{\partial \sigma}{\partial t}$$

It is clear that

$$\frac{\partial h}{\partial \sigma} = 0, \frac{\partial \eta}{\partial \sigma} = 0, \frac{\partial h}{\partial T} = \frac{\partial \eta}{\partial T}, \frac{\partial h}{\partial X} = \frac{\partial \eta}{\partial X}, \frac{\partial \sigma}{\partial z} = \frac{1}{h}$$

Therefore

$$\sigma_t = \frac{1}{h}\left(-\sigma\frac{\partial h}{\partial T}\right) = \frac{\sigma}{h}\frac{\partial}{\partial X}\left(h\int_0^1 ud\sigma\right)$$
$$\sigma_x = \frac{1}{h}\left(-\sigma\frac{\partial h}{\partial X}\right)$$
$$\sigma_z = \frac{1}{h}$$

Using the recent transformations, Eqs. (1), (5)-(6), (4) with mentioned boundary conditions are written in the new coordinates as follows, respectively

$$\frac{\partial u}{\partial X} + \sigma_x\frac{\partial u}{\partial \sigma} + \sigma_z\frac{\partial w}{\partial \sigma} = 0 \tag{10}$$

$$\frac{\partial u}{\partial T} + \sigma_t\frac{\partial u}{\partial \sigma} = -\frac{1}{\rho}\left(\frac{\partial P}{\partial X} + \sigma_x\frac{\partial p}{\partial \sigma}\right) \tag{11}$$

$$\frac{\partial w}{\partial T} + \sigma_t\frac{\partial w}{\partial \sigma} = -\frac{1}{\rho}\left(\sigma_z\frac{\partial p}{\partial \sigma}\right) \tag{12}$$

$$\frac{\partial \eta}{\partial T} - \frac{\partial}{\partial X}\left(h\int_0^1 ud\sigma\right) \tag{13}$$

Similarly, the boundary conditions are changed in new coordinates. On the wave surface we have $u_\sigma = 0, w_\sigma = 0, p = \rho g\eta$. There is a periodic condition on the left and right boundaries. At the bottom of the sea, the conditions are rewritten $u_\sigma = 0, w = 0, p_\sigma = 0$.

3.1 Finite differences scheme

In the following numerical schemes, ΔT, ΔX, and $\Delta\sigma$ are step sizes related to the T, X, and σ, nz is number of divisions and $nz+1$ is number of grid points of mesh on the vertical axis. It is worth noting that in the following indices i and k refer to node points corresponding to vertical and horizontal axis divisions, respectively. An $I \times K$ mesh of nodal

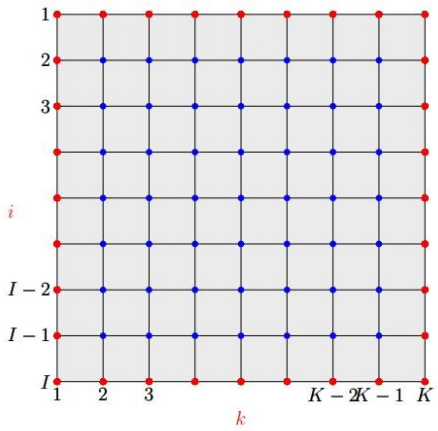

Fig. 2 Mesh in new coordinate (X, σ)

points is chosen. See Fig. 2, as it is shown in the figure, blue points are interior nodes and red ones are boundary nodes.

For Eqs. (11) and (12), horizontal and vertical velocities, it is considered

$$\left(\frac{\partial u}{\partial T}\right)^n + \left(\sigma_t \frac{\partial u}{\partial \sigma}\right)^n = -\frac{1}{2\rho}\left[\left(\frac{\partial p}{\partial X} + \sigma_x \frac{\partial p}{\partial \sigma}\right)^n + \left(\frac{\partial p}{\partial X} + \sigma_x \frac{\partial p}{\partial \sigma}\right)^{n+1}\right]$$

$$\left(\frac{\partial w}{\partial T}\right)^n + \left(\sigma_t \frac{\partial w}{\partial \sigma}\right)^n = -\frac{1}{2\rho}\left[\left(\sigma_z \frac{\partial p}{\partial \sigma}\right)^n + \left(\sigma_z \frac{\partial p}{\partial \sigma}\right)^{n+1}\right]$$

and the following numerical schemes are written

$$\frac{u_{i,k}^* - u_{i,k}^n}{\Delta T} = -\sigma_t\left(\frac{u_{i-1,k}^n - u_{i+1,k}^n}{2\Delta\sigma}\right) - \frac{1}{2\rho}\left(\frac{p_{i,k+1}^n - p_{i,k}^n}{\Delta X} + \sigma_x \frac{\frac{p_{i-1,k}^n + p_{i-1,k+1}^n}{2} - \frac{p_{i+1,k}^n + p_{i+1,k+1}^n}{2}}{2\Delta\sigma}\right) \tag{14}$$

$$\frac{u_{i,k}^{n+1} - u_{i,k}^*}{\Delta T} = -\frac{1}{2\rho}\left(\frac{p_{i,k+1}^{n+1} - p_{i,k}^{n+1}}{\Delta X} + \sigma_x \frac{\frac{p_{i-1,k}^{n+1} + p_{i-1,k+1}^{n+1}}{2} - \frac{p_{i+1,k}^{n+1} + p_{i+1,k+1}^{n+1}}{2}}{2\Delta\sigma}\right) \tag{15}$$

$$\frac{w_{i,k}^* - w_{i,k}^n}{\Delta T} = -\sigma_t \frac{w_{i-1,k}^n - w_{i+1,k}^n}{2\Delta\sigma} - \frac{1}{2\rho}\left(\sigma_z \frac{p_{i-1,k}^n - p_{i,k}^n}{\Delta\sigma}\right) \tag{16}$$

$$\frac{w_{i,k}^{n+1} - w_{i,k}^*}{\Delta T} = -\frac{1}{2\rho}\left(\sigma_z \frac{p_{i-1,k}^{n+1} - p_{i,k}^{n+1}}{\Delta\sigma}\right) \tag{17}$$

Eq. (10) for pressure leads to

$$\left(\frac{\partial^2 p}{\partial X^2} + (\sigma_x^2 + \sigma_z^2)\frac{\partial^2 p}{\partial \sigma^2} + 2\sigma_x \frac{\partial^2 p}{\partial X \partial \sigma} + \left(\frac{\partial \sigma_x}{\partial X} + \sigma_x \frac{\partial \sigma_x}{\partial \sigma}\right)\frac{\partial p}{\partial \sigma}\right)^{n+1} = \frac{2\rho}{\Delta T}\left(\frac{\partial u^*}{\partial X} + \sigma_x \frac{\partial u^*}{\partial \sigma} + \sigma_z \frac{\partial w^*}{\partial \sigma}\right)$$

that the following numerical scheme can be written

$$\begin{aligned}
&\left[\frac{p_{i,k+1}^{n+1} - 2p_{i,k}^{n+1} + p_{i,k-1}^{n+1}}{\Delta X^2} + (\sigma_x^2 + \sigma_z^2)\frac{p_{i-1,k}^{n+1} - 2p_{i,k}^{n+1} + p_{i+1,k}^{n+1}}{\Delta\sigma^2}\right. \\
&\qquad + 2\sigma_x \frac{p_{i-1,k+1}^{n+1} - p_{i-1,k-1}^{n+1} - p_{i+1,k+1}^{n+1} + p_{i+1,k-1}^{n+1}}{4\Delta X \Delta\sigma} \\
&\left. + \left(\frac{\partial \sigma_x}{\partial X} + \sigma_x \frac{\partial \sigma_x}{\partial \sigma}\right)\frac{p_{i-1,k}^{n+1} - p_{i+1,k}^{n+1}}{2\Delta\sigma}\right] \\
&= \frac{2\rho}{\Delta T}\left(\frac{u_{i,k}^* - u_{i,k-1}^*}{\Delta X} + \sigma_x \frac{\frac{u_{i-1,k-1}^* + u_{i-1,k}^*}{2} - \frac{u_{i+1,k-1}^* + u_{i+1,k}^*}{2}}{2\Delta\sigma} + \sigma_z \frac{w_{i,k}^* - w_{i+1,k}^*}{\Delta\sigma}\right)
\end{aligned}$$

This numerical scheme results in a system of linear equations as follows

$$\begin{aligned}
&c_w p_{i,k-1}^{n+1} + c_e p_{i,k+1}^{n+1} + c_s p_{i+1,k}^{n+1} + c_n p_{i-1,k}^{n+1} + c_{ws} p_{i+1,k-1}^{n+1} + c_{es} p_{i+1,k+1}^{n+1} + c_{wn} p_{i-1,k-1}^{n+1} + c_{en} p_{i-1,k+1}^{n+1} + c_o p_{i,k}^{n+1} \\
&= \frac{2\rho}{\Delta T}\left(\frac{u_{i,k}^* - u_{i,k-1}^*}{\Delta X} + \sigma_x \frac{\frac{u_{i-1,k-1}^* + u_{i-1,k}^*}{2} - \frac{u_{i+1,k-1}^* + u_{i+1,k}^*}{2}}{2\Delta\sigma} + \sigma_z \frac{w_{i,k}^* - w_{i+1,k}^*}{\Delta\sigma}\right)
\end{aligned} \tag{18}$$

In the recent system, the following relations are hold

$$c_w = c_e = \frac{\Delta\sigma}{\Delta X}$$
$$c_s = (\sigma_x^2 + \sigma_z^2)\frac{\Delta X}{\Delta\sigma} - \left(\frac{\partial\sigma_x}{\partial X} + \sigma_z\frac{\partial\sigma_x}{\partial\sigma}\right)\frac{\Delta X}{2}$$
$$c_n = (\sigma_x^2 + \sigma_z^2)\frac{\Delta X}{\Delta\sigma} + \left(\frac{\partial\sigma_x}{\partial X} + \sigma_z\frac{\partial\sigma_x}{\partial\sigma}\right)\frac{\Delta X}{2}$$
$$c_{ws} = c_{en} = \frac{\sigma_x}{2}, c_{es} = c_{wn} = -\frac{\sigma_x}{2},$$
$$c_o = -\left(\frac{2\Delta\sigma}{\Delta X} + (\sigma_x^2 + \sigma_z^2)\frac{2\Delta X}{\Delta\sigma}\right)$$

The numerical scheme for free surface elevation is

$$q_k^n = h_k^n f(z) = \sum_{i=0}^{nc} u_{i,k}^n \Delta\sigma \tag{19}$$

$$\frac{\eta_k^{n+1} - \eta_k^n}{\Delta T} = -\frac{q_k^n - q_{k-1}^n}{\Delta X} \tag{20}$$

Finally, the entire algorithm, including the steps for coordinate transformation, FD computation, and boundary condition enforcement, is summarized in Algorithm 1 for clarity and reproducibility. It is worth mentioning that the time-stepping schemes applied in the model are explicit, and the * steps are a kind of modification. In other words, the mentioned schemes split into two explicit sub-steps.

Algorithm 1: Computational Steps for Solving Ocean Wave Equations

Require: Boundary and initial conditions

Ensure: Continue till time equals final time selected by user

1. Calculate u^* and w^* at nodal points of the mesh from Eqs. (14) and (16).
2. Calculate η^{n+1} at nodal points of the surface using Eqs. (19) and (20).
3. Calculate p^{n+1} at nodal points by solving Eq. (18).
4. Calculate u^{n+1} and w^{n+1} using numerical schemes, Eqs. (15) and (17).
5. $p^0, u^0, w^0 \Leftarrow p^{n+1}, u^{n+1}, w^{n+1}$ (steps 3,4).
6. Go to step 1.

4. Numerical experiments

To assess the performance and accuracy of the proposed algorithm presented in Section 3, two numerical examples are investigated. The first example simulates deep-water wave propagation (relative depth $\frac{d}{\lambda} = 0.6$), while the second focuses on transitional wave conditions (relative depth $\frac{d}{\lambda=0.2}$). Numerical results are compared against exact analytical solutions to validate the algorithm. Root mean square error (RMSE) is calculated to measure the proximity of a numerical solution to the exact solution.

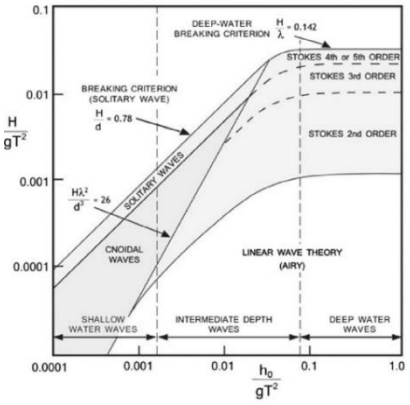

Fig. 3 Applicability ranges of various waves (Le Méhauté 2013, Maâtoug and Ayadi 2016)

$$RMSE = \sqrt{\frac{\sum_{i=1}^{N}(ya_i - ye_i)^2}{N}}$$

that ya_i, ye_i are referred to actual and evaluated values of desired quantities, respectively, and N is number of grid points in the free surface on the mesh.

In the following results, the RMSE at the free surface (upper layer) was calculated because: the main objective was to validate the wave behavior at the air-water interface, where the most critical physical processes (e.g. wave propagation, nonlinear interactions) occur. The grid was designed to ensure high resolution across the domain, and the vertical correction was dynamically adapted to maintain accuracy. The low RMSE at the free surface implicitly reflects the governing equations solved at all depths. If there is a notable error, it is propagated upwards.

4.1 Example 1: Deep-water wave case

Here, $d = 30m, \Delta\sigma = 0.02, \Delta X = 2m, \Delta T = 0.05s$. The results are shown up to one wave period. Angular frequency (ω) is obtained from the dispersion relation and wave period is determined from the relation $T = 2\pi/\omega$. The horizontal and vertical components of particle velocity at the initial, intermediate, and final time steps, $t = \Delta T, \frac{T}{2}, Ts,$ respectively, were computed using Algorithm 1, with initial conditions derived from both linear wave theory and second-order Stokes wave theory. The results, shown in Figs 4-6, demonstrate the algorithm's accuracy and stability across all time steps. At the initial time step, RMSE values were minimal, demonstrating high accuracy, with slightly better results for second-order Stokes wave theory. At the intermediate and final time steps, RMSE values increased slightly but remained acceptable, confirming the algorithm's robustness and stability throughout the simulation. At the final time step, the RMSE for the horizontal and vertical velocity components at the free surface is 7.81% and 6.21% higher, respectively, when the simulation is initialized with linear wave theory compared to second-order Stokes wave theory. This discrepancy arises because, in this example, the wave characteristics d/gT^2 = 0.0954 and h/gT^2 = 0.0032 make the second-order Stokes wave

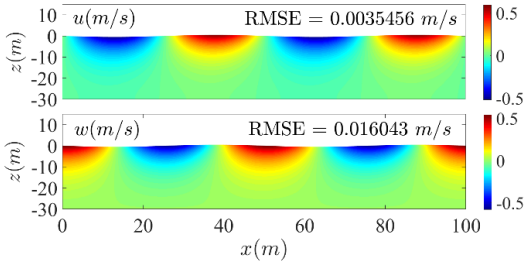

(a) Linear theory (b) second-order Stokes theory

Fig. 4 Horizontal and vertical velocity components in deep water (Example 1) at the initial time step

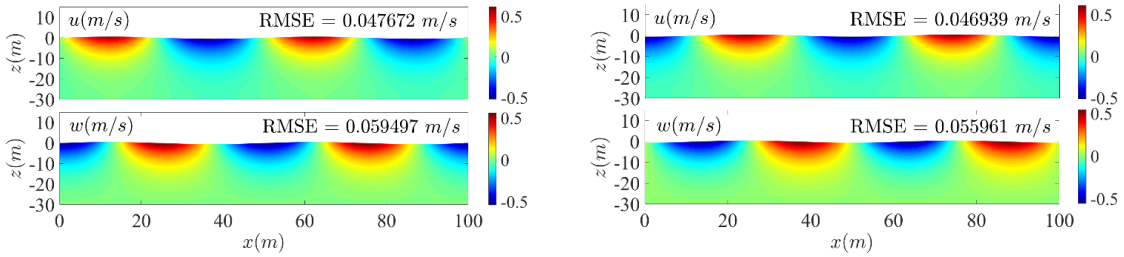

(a) Linear theory (b) second-order Stokes theory

Fig. 5 Horizontal and vertical velocity components in deep water (Example 1) at the intermediate time step

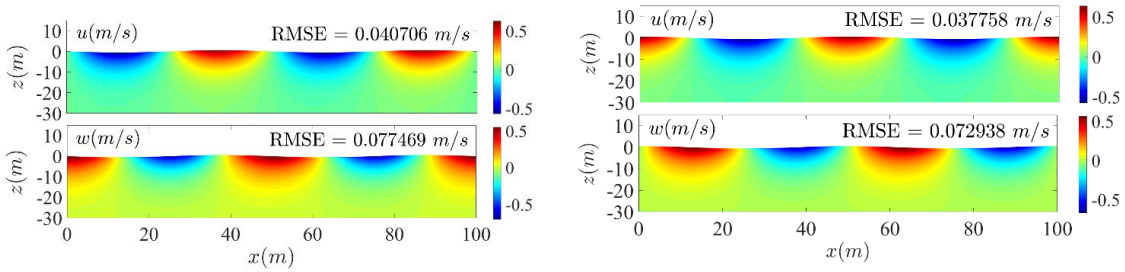

(a) Linear theory (b) second-order Stokes theory

Fig. 6 Horizontal and vertical velocity components in deep water (Example 1) at the final time step

theory a more appropriate choice for modeling (refer to Fig. 3). Fig. 7 illustrates the water surface elevation and particle positions at the final time step, providing a clear comparison between the numerical and exact solutions. The close agreement between the two highlights the algorithm's high accuracy and reliability in capturing wave dynamics. Specifically, the RMSE for the water surface elevation is 0.03885 meter when compared to linear wave theory and decreases to

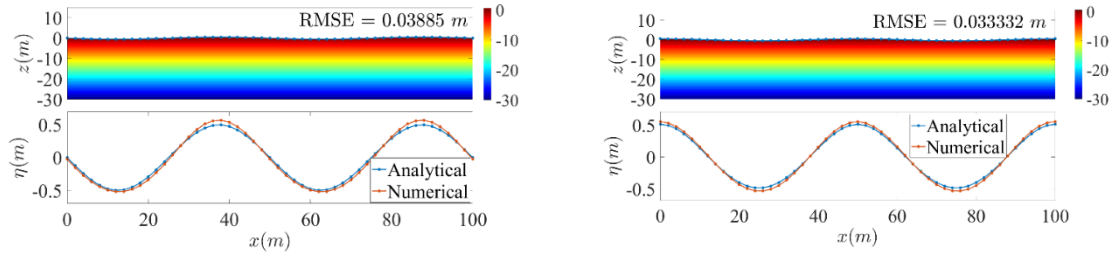

(a) Linear theory (b) second-order Stokes theory

Fig. 7 Water particle locations (top) and free surface elevation (bottom) in deep water (Example 1) at the final time step

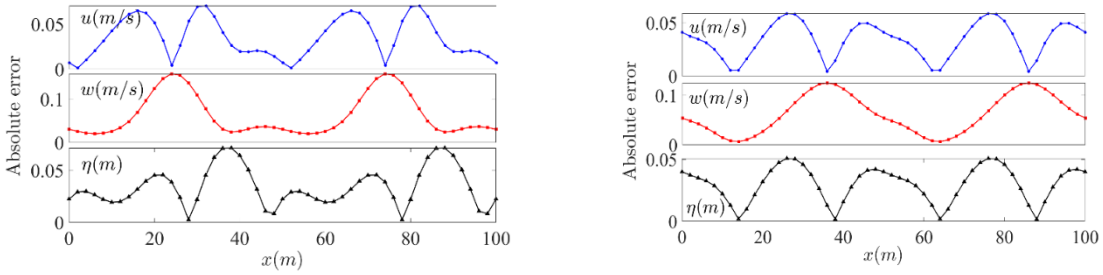

(a) Linear theory (b) second-order Stokes theory

Fig. 8 Absolute errors for u, w and η in deep water (Example 1), t= T

0.033332 meter with second-order Stokes wave theory. This reduction in RMSE (14.20%) demonstrates the improved performance of the algorithm when using second-order Stokes wave theory as the basis for initial conditions. It underscores the importance of employing higher-order wave theories to achieve more precise results, particularly for cases involving complex wave behaviors. The absolute error plots in Fig. 8 demonstrate the algorithm's precision in resolving the horizontal and vertical velocity components of water particles at the surface, as well as the wave profile, with errors remaining consistently low when compared to the exact solution. The dynamic pressure at the end of the wave period is presented in Fig. 9, accompanied by the corresponding absolute error graph at the free surface, illustrating the numerical accuracy of the simulation.

4.2 Example 2: Transitional wave case

In this example,$d = 10\ m, \Delta\sigma = 0.02, \Delta X = 2\ m, \Delta T = 0.06s$, and the wave parameters are d/gT^2=0.0271 and H/gT^2=0.0027. The results are presented up to one wave period. Again, angular frequency (ω) is obtained from the dispersion relation and wave period is $T = 2\pi/\omega$. The algorithm's accuracy was evaluated by comparing RMSE values at the initial, intermediate, and final time steps, $t = \Delta T, T/2, T\ s,$ respectively, with predictions from linear and second-order Stokes wave theories (Figs. 10-12). At the initial step, the algorithm demonstrated high precision.

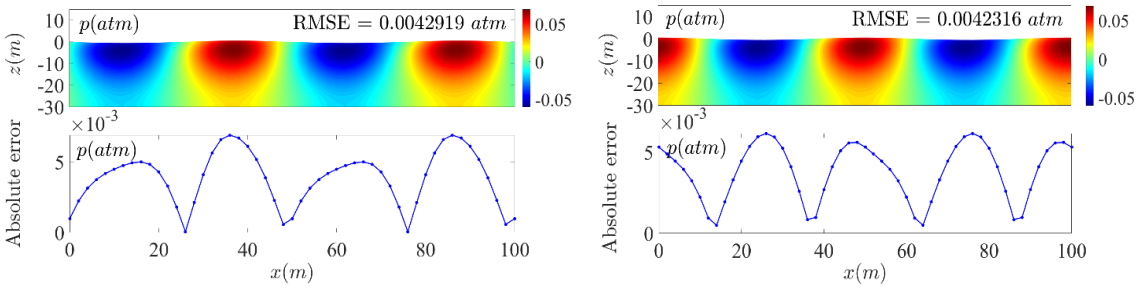

(a) Linear theory (b) second-order Stokes theory

Fig. 9 Dynamic pressure (top) and absolute error for p (bottom) in deep water (Example 1), $t = T$

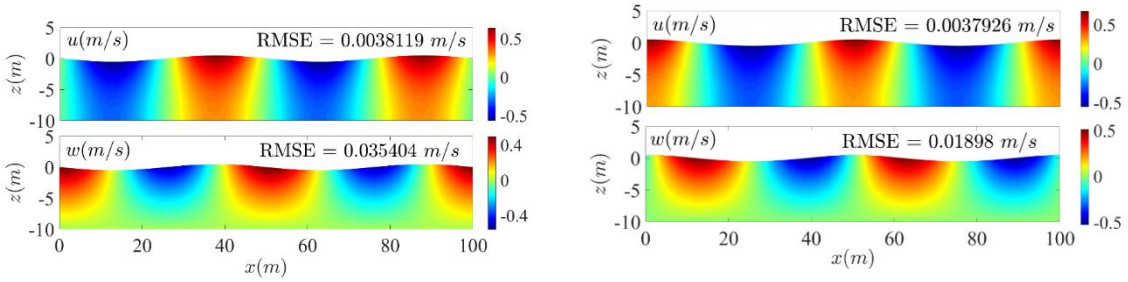

(a) Linear theory (b) second-order Stokes theory

Fig. 10 Horizontal and vertical velocity components in transitional water (Example 2) at the initial time step

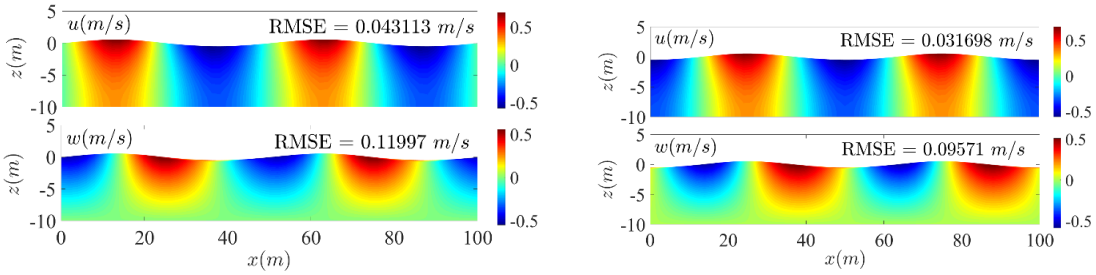

(a) Linear theory (b) second-order Stokes theory

Fig. 11 Horizontal and vertical velocity components in transitional water (Example 2) at the intermediate time step

Although RMSE values increased at later steps, they remained within RMSE $\leq$ 0.15 m/s, confirming the algorithm's stability and reliability in modeling transitional wave behavior. As depicted in Fig. 11, employing second-order Stokes wave theory reduces the RMSE of horizontal

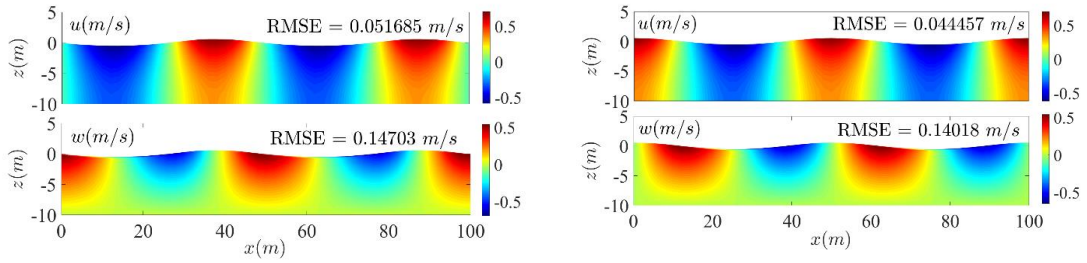

(a) Linear theory (b) second-order Stokes theory

Fig. 12 Horizontal and vertical velocity components in transitional water (Example 2) at the final time step

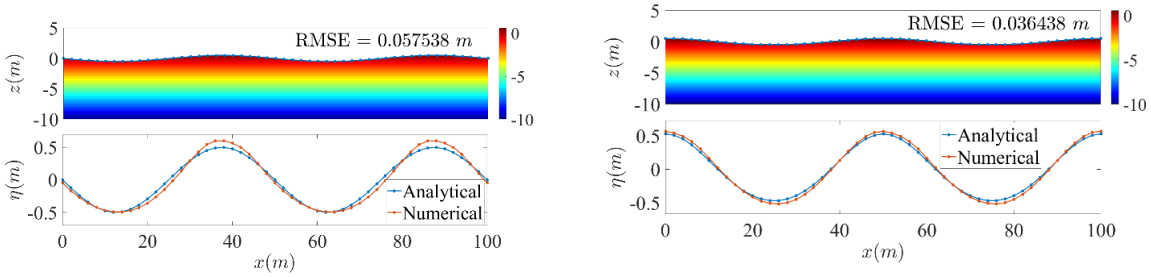

(a) Linear theory (b) second-order Stokes theory

Fig. 13 Water particle locations (top) and free surface elevation (bottom) in transitional water (Example 2) at the final time step

and vertical velocity components at the free water surface by 26.48% and 20.22%, respectively, at the intermediate time step, compared to linear wave theory. This reduction is attributed to the complexity of wave behavior under transitional conditions, where the second-order Stokes wave theory more accurately describes the wave dynamics. Fig. 13 provides a detailed evaluation of the algorithm's accuracy in modeling water surface elevation and particle positions at the final time step. The RMSE values, calculated as 0.057538 meter for linear wave theory and 0.036438 meter for second-order Stokes wave theory, highlight the algorithm's precision. The lower error associated with the second-order Stokes theory reflects the algorithm's ability to effectively capture nonlinear wave effects. In Fig. 14, the absolute error for the horizontal and vertical velocity components (u and w) at the water surface, along with the wave profile, is shown. Fig. 14(a) compares results with linear wave theory, while Fig. 14(b) presents comparisons with second-order Stokes wave theory. The absolute errors for both velocity components and the wave profile are minimal, with a periodic distribution that closely follows wave dynamics. In panel Fig. 14(b), the errors are notably smaller, particularly for the horizontal velocity component, where the peak errors are reduced compared to Fig. 14(a). This indicates the algorithm's enhanced accuracy in capturing nonlinear wave effects. The consistent periodicity of the error across the wave profile further underscores the algorithm's stability and reliability in modeling wave behavior, even under transitional wave conditions. Fig. 15 presents the dynamic pressure at the wave period's conclusion, accompanied by the corresponding absolute error profile at the free surface.

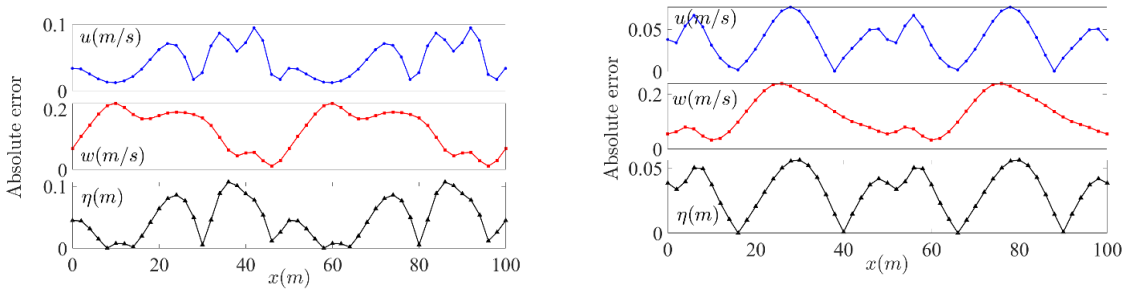

(a) Linear theory (b) second-order Stokes theory

Fig. 14 Absolute errors for u, w and η in transitional water (Example 2), t= T

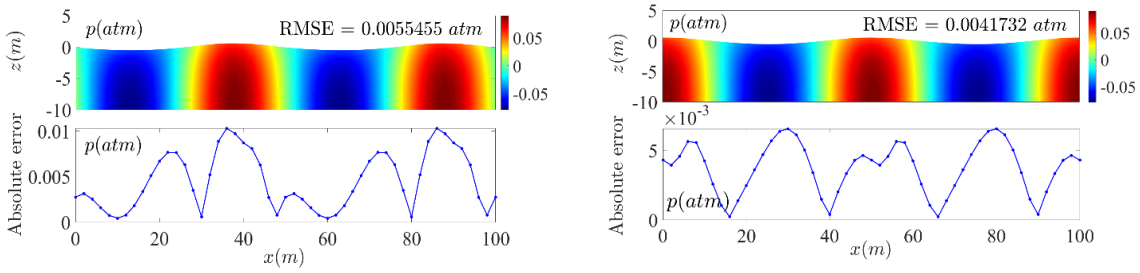

(a) Linear theory (b) second-order Stokes theory

Fig. 15 Dynamic pressure (top) and absolute error for p (bottom) in transitional water (Example 2), t= T

Also, simulations were conducted for up to 5 wave periods under both deep water and transitional water conditions, and the results were found to remain stable with bounded errors and no significant accumulation of errors over time. For example, the NRMSE (Normalized Root Mean Square Error) of the free surface elevation remains from about 7.36% to below 10% throughout the simulations, and other variables follow a similar trend. Given the consistency and stability observed, it can be concluded the current results sufficiently demonstrate the long-term accuracy. It is also important to note that in numerical simulations, some increase in error over time is natural and expected due to the inherent accumulation of numerical approximations. However, what matters is not the complete elimination of error, but ensuring that it remains bounded, stable, and within an acceptable range that the present results confirm that the model performs reliably within the simulated and reasonable time frame.

4.3 Stability and consistency analysis

The agreement and similarity observed in the velocity component profiles indicate the stability of the proposed numerical scheme, with no signs of error growth over time. Stability, a crucial property of any numerical method, ensures that computational errors remain bounded and do not propagate uncontrollably as simulations progress. The stability of the proposed scheme was assessed by keeping the spatial step size constant at 2 meters, while varying the time step size from

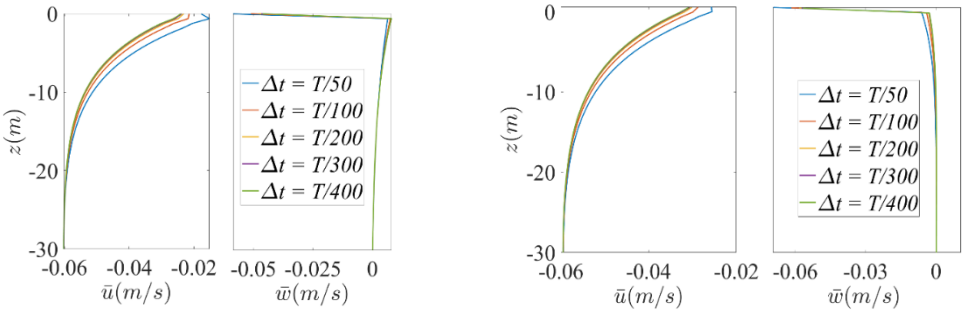

(a) Linear theory (b) second-order Stokes theory

Fig. 16 Velocity components profile in deep water, *t*= *T*

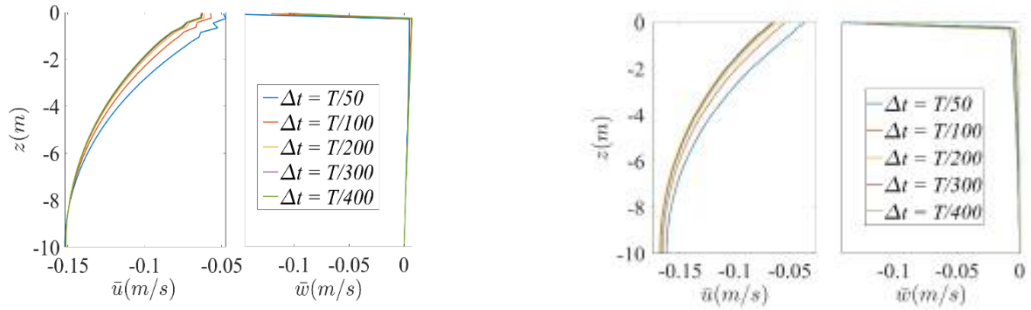

(a) Linear theory (b) second-order Stokes theory

Fig. 17 Velocity components profile in transitional water, *t*= *T*

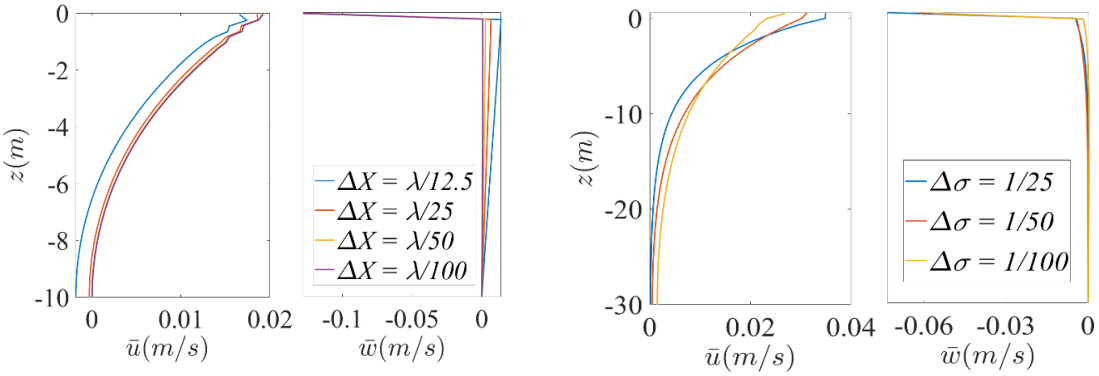

(a) Transitional water, linear theory (b) Deep water, second-order Stokes theory

Fig. 18 Velocity components profile, *t*= *T*

T/50 to *T*/400. These time steps correspond approximately to $\Delta t = 0.1,0.05,0.03,0.02,0.01$ in deep water, and $\Delta t = 0.1,0.06,0.03,0.02,0.01$ in transitional water, as shown in Figs. 16 and 17. The results clearly demonstrate that the algorithm provides stable solutions across a wide range of time step sizes, further validating its robustness. To ensure the consistency of the numerical

scheme, a rigorous proof provided in Appendix A uses Taylor series expansions to approximate particle velocities and pressures at different spatial and temporal positions. This proof shows that as the spatial (ΔX) and temporal ($\Delta\sigma$) step sizes approach zero, the finite-difference-based estimator equations converge to the original governing equations of the physical system. In addition, a similar sensitivity analysis was performed for ΔX and $\Delta\sigma$, in transitional and deep-water wave cases, respectively. As illustrated in Fig. 18, a careful examination reveals that while both cases exhibit overall convergence, the sensitivity is slightly higher for the choice of $\Delta\sigma$. This convergence guarantees that the numerical scheme faithfully represents the underlying physical model, maintaining accuracy even with finer discretization. As a result, this numerical procedure offers a reliable framework for solving similar problems, especially when analytical or exact solutions are not available. Its proven stability and consistency make it a dependable tool for obtaining converged numerical solutions in practical applications.

4.4 Limitations and challenges

Despite the versatility of sigma-coordinate transformations coupled with finite-difference schemes, several inherent limitations and computational challenges remain that must be addressed in future developments:

1. Depth and wave-height constraints

Most sigma-based models assume moderate to deep-water conditions and may lose accuracy in very shallow or extremely deep regions where the mapping becomes highly distorted. In real-world applications, bathymetric variability and extreme wave events (e.g., storm surges) can violate these assumptions, limiting the model's applicability to specific relative depth regimes. In truly shallow-water conditions, where nonlinear terms and wave breaking become dominant, the present linearized model must be augmented with nonlinear advection, dispersion correction, and possibly shock-capturing schemes to ensure physical realism.

2. Simplified physics and boundary representations

To maintain tractability, many models neglect or linearize processes such as wind-wave coupling, bottom friction, and turbulent convection at the free surface (Warner *et al*. 2005). Such simplifications can under-represent energy dissipation and interfacial momentum exchange, key mechanisms in coupled ocean, atmosphere systems.

3. Structured grids and two-dimensionality

Reliance on vertically stretched, structured meshes restricts the model to 2D formulations; this precludes fully resolving three-dimensional wave phenomena such as oblique shoaling, rip currents, and wave–current interactions without substantial grid refinement or regridding overhead (Chen *et al.* 2003).

4. High computational cost

Nonlinear wave dynamics and multi-scale coupling (e.g., wave–atmosphere feedbacks) impose severe demands on CPU time and memory. Long-duration simulations or large domains can become prohibitively expensive, especially when high resolution is required for stability (Zhang and Baptista 2008).

5. Error propagation and long-term stability

Finite-difference discretizations are prone to cumulative truncation and round-off errors over extended integration periods. Without careful time-step control and filtering, numerical instabilities may emerge, compromising solution fidelity. Long-term simulations require greater care in numerical schemes and interpretation, as certain simplifications that are valid for

short-term analysis may introduce noticeable deviations over extended periods.

6. Interface dynamics modeling

Accurately capturing the coupling between the ocean surface and overlying atmosphere remains a fundamental challenge. Grid-mapping artifacts near the free surface and the enforcement of boundary conditions across two dynamically coupled media can introduce spurious reflections or energy leakage (Warner *et al*. 2008).

Addressing these limitations will involve (a) implementing adaptive, unstructured meshes to better capture bathymetric complexity, (b) incorporating higher-order or conservative nonlinear operators for shallow regimes, and (c) developing efficient parallel algorithms to reduce computational cost. These enhancements will pave the way for robust, fully coupled ocean–atmosphere simulations in future work.

5. Conclusions

This study presents a comprehensive numerical framework for simulating ocean wave propagation using an integrated σ-transformation and finite difference (FD) method. The proposed algorithm demonstrates strong accuracy, stability, and consistency in modeling both deep-water and transitional wave conditions. By employing a coordinate transformation, the method effectively handles irregular physical domains and boundary conditions, ensuring efficient and reliable solutions for complex wave dynamics. The numerical experiments conducted with deep-water and transitional wave cases show that the algorithm provides high precision at all time steps, with RMSE values remaining within acceptable limits. The comparison between linear and second-order Stokes wave theories further highlights the algorithm's ability to capture nonlinear wave effects, with significant reductions in error when the second-order Stokes theory is employed.

This indicates the method's robustness in dealing with the complexities of wave behavior under various conditions. Additionally, the stability analysis confirms that the proposed scheme is capable of providing stable solutions across a broad range of time step sizes, with no indication of error growth over time. The consistency of the numerical scheme is rigorously demonstrated through a proof of convergence, ensuring that the method maintains accuracy as the spatial and temporal discretization become finer. Overall, this research provides a valuable tool for simulating complex ocean wave dynamics, particularly in environments where analytical solutions are difficult to obtain. The proven reliability, stability, and consistency of the algorithm make it a powerful resource for future studies and practical applications in marine engineering, hydrodynamics, and coastal management.

References

Agarwal, S., Sriram, V., Liu, P.F. and Murali, K. (2022), "Waves in waterways generated by moving pressure field in Boussinesq equations using unstructured finite element model", *Ocean Eng*., **262**, 112202. https://doi.org/10.1016/j.oceaneng.2022.112202.

Bakhoday-Paskyabi, M. (2015), "Particle motions beneath irrotational water waves", *Ocean Dynam*., **65**, 1063-1078. https://doi.org/10.1007/s10236-015-0856-4.

Bakhoday-Paskyabi, M. (2017), "Wavelet Galerkin scheme for solving nonlinear dispersive shallow water

waves: Application in bore propagation and breaking", *Wave Motion*, **73**, 24-44. https://doi.org/10.1016/j.wavemoti.2017.04.009.
Benkhaldoun, F. and Seaïd, M. (2010), "A simple finite volume method for the shallow water equations", *J. Comput. Appl. Math*., **234**, 58-72. https://doi.org/10.1016/j.cam.2009.12.005.
Chen, C., Liu, H. and Beardsley, R.C. (2003), "An unstructured grid, finite-volume, three-dimensional, primitive equations ocean model: application to coastal ocean and estuaries", *J. Atmos. Ocean. Technol.*, **20**(1), 159-186. https://doi.org/10.1175/1520-0426(2003)020<0159:AUGFVT>2.0.CO;2.
Ghoneim, A.Y. (2025), "Meshfree phase-field modeling of three-phase flow using smoothed particle hydrodynamics with differential reproducing kernels and artificial compressibility", *J. Comput. Appl. Math*., **469**, 116654. https://doi.org/10.1016/j.cam.2025.116654.
Khater, M.M. (2023), "Computational simulations of propagation of a tsunami wave across the ocean", *Chaos Solit. Fractals*, **174**, 113806. https://doi.org/10.1016/j.chaos.2023.113806.
Klahn, M., Madsen, P.A. and Fuhrman, D.R. (2020), "A new σ-transform based Fourier-Legendre-Galerkin model for nonlinear water waves", *Int. J. Numer. Meth. Fl.*, **93**, 220-248. https://doi.org/10.1002/fld.4881.
Kumar, P. (2018), "Modeling of shallow water waves with variable bathymetry in an irregular domain by using hybrid finite element method", *Ocean Eng*., **165**, 386-398. https://doi.org/10.1016/j.oceaneng.2018.07.024.
Kurt, A., Tozar, A. and Tasbozan, O. (2020), "Applying the new extended direct algebraic method to solve the equation of obliquely interacting waves in shallow waters", *J. Ocean Univ. China*, **19**, 772-780. https://doi.org/10.1007/s11802-020-4135-8.
Le Méhauté, B. (2013), "An introduction to hydrodynamics and water waves", *Springer Science & Business Media*.
Lin, P. and Li, C.W. (2002), "A σ-coordinate three-dimensional numerical model for surface wave propagation", *Int. J. Numer. Meth. Fl*., **38**, 1045-1068. https://doi.org/10.1002/fld.258.
Liu, M.B. and Liu, G.R. (2010), "Smoothed Particle Hydrodynamics (SPH): an Overview and Recent Developments", *Arch. Comput. Method. Eng.*, **17**, 25-76. https://doi.org/10.1007/s11831-010-9040-7.
Lundgren, L. and Mattsson, K. (2020), "An efficient finite difference method for the shallow water equations", *J. Comput. Phys*., **422**, 109784. https://doi.org/10.1016/j.jcp.2020.109784.
Maâtoug, M.A. and Ayadi, M. (2016), "Numerical simulation of the second-order Stokes theory using finite difference method", *Alex. Eng. J*., **55**, 3005-3013. https://doi.org/10.1016/j.aej.2016.04.035.
Monaghan, J.J., (1994), "Simulating free surface flows with SPH", *J. Comput. Phys*., **110**(2), 399-406. https://doi.org/10.1006/jcph.1994.1034.
Ning, X., Paskyabi, M.B., Bui, H.H. and Penchah, M.M. (2023), "Evaluation of sea surface roughness parameterization in meso-to-micro scale simulation of the offshore wind field", *J. Wind Eng. Ind. Aerod*., **242**, 105592. https://doi.org/10.1016/j.jweia.2023.105592.
Paskyabi, M.B. (2016), "Turbulence-particle interactions under surface gravity waves", *Ocean Dyn*., **66**, 1429-1448. https://doi.10.1007/s10236-016-0989-0.
Qi, Y., Söding, H., el Moctar, O., Neugebauer, J. and Schellin, T. (2024), "A three-dimensional fully linear finite difference approach to predict waves in tanks excited by ship motions", *Ocean Eng*., **302**, 117391. https://doi.org/10.1016/j.oceaneng.2024.117391.
Shirkavand, A. and Farrahi-Moghaddam, K. (2024), "A non-hydrostatic numerical model for simulating regular wave breaking and surf-swash zone motions", *Sci. Rep*., **14**, 9729. https://doi.org/10.1038/s41598-024-60470-3.
Turnbull, M.S., Borthwick, A.G.L. and Taylor, R.E. (2003), "Numerical wave tank based on a σ-transformed finite element inviscid flow solver", *Int. J. Numer. Meth. Fl*., **42**, 641-663. https://doi.org/10.1002/fld.539.
Wang, X. and Liu, P.L.F. (2011), "An explicit finite difference model for simulating weakly nonlinear and weakly dispersive waves over slowly varying water depth", *Coast. Eng*., **58**, 173-183. https://doi.org/10.1016/j.coastaleng.2010.09.008.
Warner, J.C., Perlin, N. and Skyllingstad, E.D. (2008), "Using the model coupling toolkit to couple earth

system models", *Environ. Model. Softw.*, **23**(10-11), 1240-1249. https://doi.org/10.1016/j.envsoft.2008.03.002.

Warner, J.C., Sherwood, C.R., Arango, H.G. and Signell, R.P. (2005), "Performance of four turbulence closure models implemented using a generic length scale method", *Ocean Model.,* **8**(1-2), 81-113. https://doi:10.1016/j.ocemod.2003.12.003.

Wei, Z. and Jia, Y. (2014), "Simulation of nearshore wave processes by a depth-integrated non-hydrostatic finite element model", *Coast. Eng*., **83**, 93-107. https://doi.org/10.1016/j.coastaleng.2013.10.002.

Xu, Y., Bingham, H.B. and Shao, Y. (2021), "Finite difference solutions for nonlinear water waves using an immersed boundary method", *Int. J. Numer. Meth. Fl*., **93**, 1143-1162. https://doi.org/10.1002/fld.4922.

Yang, S., Zhu, X. and Ren, H. (2024), "A two-dimensional σ-transform based finite element method for nonlinear water waves", *Ocean. Eng*., **308**, 118299. https://doi.org/10.1016/j.oceaneng.2024.118299.

Zhang, Y. and Baptista, A.M. (2008), "SELFE: A semi-implicit Eulerian–Lagrangian finite-element model for cross-scale ocean circulation", *Ocean Model*., **21**(3-4), 71-96. https://doi:10.1016/j.ocemod.2007.11.005

Zheng, P.B. and Zhang, H.S. (2024), "2DH numerical model of nonlinear wave propagation based on a hybrid finite-volume and finite-difference scheme", *Appl. Ocean Res*., **148**, 104008. https://doi.org/10.1016/j.apor.2024.104008.

Zhu, B., Hiraishi, T., Mase, H., Pei, H. and Yang, Q. (2022), "Probabilistic analysis of wave-induced dynamic response in a pyroclastic sloping seabed using random finite element method", *Ocean Eng*., **252**, 111231. https://doi.org/10.1016/j.oceaneng.2022.111231.

MK

Appendix A. Consistency

In order to prove the consistency of numerical schemes, one-variable and two-variable Taylor formulas result in:

$$u_{i-1,k}^{n} = u_{i,k}^{n} + \Delta\sigma \frac{\partial u_{i,k}^{n}}{\partial \sigma} + \frac{(\Delta\sigma)^2}{2!} \frac{\partial^2 u_{i,k}^{n}}{\partial \sigma^2} + \frac{(\Delta\sigma)^3}{3!} \frac{\partial^3 u_{i,k}^{n}}{\partial \sigma^3} + O((\Delta\sigma)^4)$$

$$u_{i+1,k}^{n} = u_{i,k}^{n} - \Delta\sigma \frac{\partial u_{i,k}^{n}}{\partial \sigma} + \frac{(\Delta\sigma)^2}{2!} \frac{\partial^2 u_{i,k}^{n}}{\partial \sigma^2} - \frac{(\Delta\sigma)^3}{3!} \frac{\partial^3 u_{i,k}^{n}}{\partial \sigma^3} + O((\Delta\sigma)^4)$$

$$p_{i,k+1}^{n} = p_{i,k}^{n} + \Delta X \frac{\partial p_{i,k}^{n}}{\partial X} + \frac{(\Delta X)^2}{2!} \frac{\partial^2 p_{i,k}^{n}}{\partial X^2} + \frac{(\Delta X)^3}{3!} \frac{\partial^3 p_{i,k}^{n}}{\partial X^3} + O((\Delta X)^4)$$

$$p_{i-1,k}^{n} = p_{i,k}^{n} + \Delta\sigma \frac{\partial p_{i,k}^{n}}{\partial \sigma} + \frac{(\Delta\sigma)^2}{2!} \frac{\partial^2 p_{i,k}^{n}}{\partial \sigma^2} + \frac{(\Delta\sigma)^3}{3!} \frac{\partial^3 p_{i,k}^{n}}{\partial \sigma^3} + O((\Delta\sigma)^4)$$

$$\begin{aligned} p_{i-1,k+1}^{n} = p_{i,k}^{n} &+ \Delta\sigma \frac{\partial p_{i,k}^{n}}{\partial \sigma} + \Delta X \frac{\partial p_{i,k}^{n}}{\partial X} + \frac{1}{2!}\left((\Delta\sigma)^2 \frac{\partial^2 p_{i,k}^{n}}{\partial \sigma^2} + 2\Delta\sigma\Delta X \frac{\partial^2 p_{i,k}^{n}}{\partial \sigma \partial X} + (\Delta X)^2 \frac{\partial^2 p_{i,k}^{n}}{\partial X^2} \right) \\ &+ \frac{1}{3!}\left((\Delta\sigma)^3 \frac{\partial^3 p_{i,k}^{n}}{\partial \sigma^3} + 3(\Delta\sigma)^2 \Delta X \frac{\partial^3 p_{i,k}^{n}}{\partial \sigma^2 \partial X} + 3(\Delta X)^2 \Delta\sigma \frac{\partial^3 p_{i,k}^{n}}{\partial \sigma \partial X^2} + (\Delta X)^3 \frac{\partial^3 p_{i,k}^{n}}{\partial X^3} \right) \\ &+ O\left((\Delta\sigma)^4, (\Delta X)^4, (\Delta\sigma)^3 \Delta X, (\Delta X)^3 \Delta\sigma, (\Delta\sigma)^2 (\Delta X)^2 \right) \end{aligned}$$

$$p_{i+1,k}^{n} = p_{i,k}^{n} - \Delta\sigma \frac{\partial p_{i,k}^{n}}{\partial \sigma} + \frac{(\Delta\sigma)^2}{2!} \frac{\partial^2 p_{i,k}^{n}}{\partial \sigma^2} - \frac{(\Delta\sigma)^3}{3!} \frac{\partial^3 p_{i,k}^{n}}{\partial \sigma^3} + O((\Delta\sigma)^4)$$

$$\begin{aligned} p_{i+1,k+1}^{n} = p_{i,k}^{n} &- \Delta\sigma \frac{\partial p_{i,k}^{n}}{\partial \sigma} + \Delta X \frac{\partial p_{i,k}^{n}}{\partial X} + \frac{1}{2!}\left((\Delta\sigma)^2 \frac{\partial^2 p_{i,k}^{n}}{\partial \sigma^2} - 2\Delta\sigma\Delta X \frac{\partial^2 p_{i,k}^{n}}{\partial \sigma \partial X} + (\Delta X)^2 \frac{\partial^2 p_{i,k}^{n}}{\partial X^2} \right) \\ &+ \frac{1}{3!}\left(-(\Delta\sigma)^3 \frac{\partial^3 p_{i,k}^{n}}{\partial \sigma^3} + 3(\Delta\sigma)^2 \Delta X \frac{\partial^3 p_{i,k}^{n}}{\partial \sigma^2 \partial X} - 3(\Delta X)^2 \Delta\sigma \frac{\partial^3 p_{i,k}^{n}}{\partial \sigma \partial X^2} + (\Delta X)^3 \frac{\partial^3 p_{i,k}^{n}}{\partial X^3} \right) \\ &+ O\left((\Delta\sigma)^4, (\Delta X)^4, (\Delta\sigma)^3 \Delta X, (\Delta X)^3 \Delta\sigma, (\Delta\sigma)^2 (\Delta X)^2 \right) \end{aligned}$$

and

$$p_{i,k+1}^{n+1} = p_{i,k}^{n+1} + \Delta X \frac{\partial p_{i,k}^{n+1}}{\partial X} + \frac{(\Delta X)^2}{2!} \frac{\partial^2 p_{i,k}^{n+1}}{\partial X^2} - \frac{(\Delta X)^3}{3!} \frac{\partial^3 p_{i,k}^{n+1}}{\partial X^3} + O((\Delta X)^4).$$

Similar relations can also be obtained per time step $n+1$. It can be clearly inferred that when $\Delta X \to 0, \Delta\sigma \to 0$, the following relations are concluded:

$$-\sigma_t \frac{u_{i-1,k}^{n} - u_{i+1,k}^{n}}{2\Delta\sigma} = \frac{-\sigma_t}{2\Delta\sigma}\left(2\Delta\sigma \frac{\partial u_{i,k}^{n}}{\partial \sigma} + 2\frac{(\Delta\sigma)^3}{3!} \frac{\partial^3 u_{i,k}^{n}}{\partial \sigma^3} + O((\Delta\sigma)^5) \right) \to -\sigma_t \frac{\partial u_{i,k}^{n}}{\partial \sigma}$$

$$\frac{p_{i,k+1}^n - p_{i,k}^n}{\Delta X} = \frac{1}{\Delta X}\left(\Delta X \frac{\partial p_{i,k}^n}{\partial X} + \frac{(\Delta X)^2}{2!}\frac{\partial^2 p_{i,k}^n}{\partial X^2} + O((\Delta X)^3)\right) \to \frac{\partial p_{i,k}^n}{\partial X}$$

$$\frac{p_{i-1,k}^n + p_{i-1,k+1}^n}{2} = \frac{1}{2}\left(2p_{i,k}^n + 2\Delta\sigma\frac{\partial p_{i,k}^n}{\partial\sigma} + 2\frac{(\Delta\sigma)^2}{2!}\frac{\partial^2 p_{i,k}^n}{\partial\sigma^2} + \Delta X\frac{\partial p_{i,k}^n}{\partial X} + \Delta\sigma\Delta X\frac{\partial^2 p_{i,k}^n}{\partial\sigma\partial X} + \frac{1}{2}(\Delta X)^2\frac{\partial^2 p_{i,k}^n}{\partial X^2} + O\left((\Delta\sigma)^3,(\Delta X)^3,(\Delta X)^2\Delta\sigma,(\Delta\sigma)^2\Delta X\right)\right)$$

$$\frac{p_{i+1,k}^n + p_{i+1,k+1}^n}{2} = \frac{1}{2}\left(2p_{i,k}^n - 2\Delta\sigma\frac{\partial p_{i,k}^n}{\partial\sigma} + 2\frac{(\Delta\sigma)^2}{2!}\frac{\partial^2 p_{i,k}^n}{\partial\sigma^2} + \Delta X\frac{\partial p_{i,k}^n}{\partial X} - \Delta\sigma\Delta X\frac{\partial^2 p_{i,k}^n}{\partial\sigma\partial X} + \frac{1}{2}(\Delta X)^2\frac{\partial^2 p_{i,k}^n}{\partial X^2} + O\left((\Delta\sigma)^3,(\Delta X)^3,(\Delta X)^2\Delta\sigma,(\Delta\sigma)^2\Delta X\right)\right)$$

and hence

$$\frac{\frac{p_{i-1,k}^n + p_{i-1,k+1}^n}{2} - \frac{p_{i+1,k}^n + p_{i+1,k+1}^n}{2}}{2\Delta\sigma} \to \frac{\partial p_{i,k}^n}{\partial\sigma}$$

$$-\frac{1}{2\rho}\left(\frac{p_{i,k+1}^n - p_{i,k}^n}{\Delta X} + \sigma_x\frac{\frac{p_{i-1,k}^n + p_{i-1,k+1}^n}{2} - \frac{p_{i+1,k}^n + p_{i+1,k+1}^n}{2}}{2\Delta\sigma}\right) \to -\frac{1}{2\rho}\left(\frac{\partial p_{i,k}^n}{\partial X} + \sigma_x\frac{\partial p_{i,k}^n}{\partial\sigma}\right)$$

and similarly, relations for the time step $n+1$ can be written. With a little simplification, the following relations are obtained that show the consistency of the numerical scheme for the horizontal velocity equation.

$$\left(\frac{\partial u}{\partial T}\right)^n = \frac{u_{i,k}^{n+1} - u_{i,k}^*}{\Delta T} + \frac{u_{i,k}^* - u_{i,k}^n}{\Delta T} = -\frac{1}{2\rho}\left(\frac{\partial p_{i,k}^n}{\partial X} + \sigma_x\frac{\partial p_{i,k}^n}{\partial\sigma} + \frac{\partial p_{i,k}^{n+1}}{\partial X} + \sigma_x\frac{\partial p_{i,k}^{n+1}}{\partial\sigma}\right) - \sigma_t\frac{\partial u_{i,k}^n}{\partial\sigma}$$

also, from the following relations

$$w_{i-1,k}^n = w_{i,k}^n + \Delta\sigma\frac{\partial w_{i,k}^n}{\partial\sigma} + \frac{(\Delta\sigma)^2}{2!}\frac{\partial^2 w_{i,k}^n}{\partial\sigma^2} + \frac{(\Delta\sigma)^3}{3!}\frac{\partial^3 w_{i,k}^n}{\partial\sigma^3} + O((\Delta\sigma)^4)$$

$$w_{i+1,k}^n = w_{i,k}^n - \Delta\sigma\frac{\partial w_{i,k}^n}{\partial\sigma} + \frac{(\Delta\sigma)^2}{2!}\frac{\partial^2 w_{i,k}^n}{\partial\sigma^2} - \frac{(\Delta\sigma)^3}{3!}\frac{\partial^3 w_{i,k}^n}{\partial\sigma^3} + O((\Delta\sigma)^4)$$

$$p_{i-1,k}^n = p_{i,k}^n + \Delta\sigma\frac{\partial p_{i,k}^n}{\partial\sigma} + \frac{(\Delta\sigma)^2}{2!}\frac{\partial^2 p_{i,k}^n}{\partial\sigma^2} + \frac{(\Delta\sigma)^3}{3!}\frac{\partial^3 p_{i,k}^n}{\partial\sigma^3} + O((\Delta\sigma)^4)$$

and

$$p_{i-1,k}^{n+1} = p_{i,k}^{n+1} + \Delta\sigma\frac{\partial p_{i,k}^{n+1}}{\partial\sigma} + \frac{(\Delta\sigma)^2}{2!}\frac{\partial^2 p_{i,k}^{n+1}}{\partial\sigma^2} + \frac{(\Delta\sigma)^3}{3!}\frac{\partial^3 p_{i,k}^{n+1}}{\partial\sigma^3} + O((\Delta\sigma)^4)$$

it can be written

$$\frac{w_{i-1,k}^{n}-w_{i+1,k}^{n}}{2\Delta\sigma}=\frac{1}{2\Delta\sigma}\left(2\Delta\sigma\frac{\partial w_{i,k}^{n}}{\partial\sigma}+2\frac{(\Delta\sigma)^{3}}{3!}\frac{\partial^{3}w_{i,k}^{n}}{\partial\sigma^{3}}+O((\Delta\sigma)^{5})\right)\rightarrow\frac{\partial w_{i,k}^{n}}{\partial\sigma}$$

and

$$\frac{p_{i-1,k}^{n}-p_{i,k}^{n}}{\Delta\sigma}=\frac{1}{\Delta\sigma}\left(\Delta\sigma\frac{\partial p_{i,k}^{n}}{\partial\sigma}+\frac{(\Delta\sigma)^{2}}{2!}\frac{\partial^{2}p_{i,k}^{n}}{\partial\sigma^{2}}+O((\Delta\sigma)^{3})\right)\rightarrow\frac{\partial p_{i,k}^{n}}{\partial\sigma}$$

and hence

$$-\sigma_{t}\frac{w_{i-1,k}^{n}-w_{i+1,k}^{n}}{2\Delta\sigma}=-\sigma_{t}\left(\frac{\partial w_{i,k}^{n}}{\partial\sigma}+\frac{(\Delta\sigma)^{2}}{3!}\frac{\partial^{3}w_{i,k}^{n}}{\partial\sigma^{3}}+O((\Delta\sigma)^{4})\right)\rightarrow-\sigma_{t}\frac{\partial w_{i,k}^{n}}{\partial\sigma}$$

and

$$-\frac{1}{2\rho}\left(\sigma_{z}\frac{p_{i-1,k}^{n}-p_{i,k}^{n}}{\Delta\sigma}\right)=-\frac{\sigma_{z}}{2\rho}\left(\frac{\partial p_{i,k}^{n}}{\partial\sigma}+\frac{\Delta\sigma}{2!}\frac{\partial^{2}p_{i,k}^{n}}{\partial\sigma^{2}}+O((\Delta\sigma)^{2})\right)\rightarrow-\frac{\sigma_{z}}{2\rho}\frac{\partial p_{i,k}^{n}}{\partial\sigma}$$

so

$$\frac{w_{i,k}^{*}-w_{i,k}^{n}}{\Delta T}=-\sigma_{t}\frac{\partial w_{i,k}^{n}}{\partial\sigma}-\frac{\sigma_{z}}{2\rho}\frac{\partial p_{i,k}^{n}}{\partial\sigma}$$

and

$$\frac{w_{i,k}^{n+1}-w_{i,k}^{*}}{\Delta T}=-\frac{1}{2\rho}\sigma_{z}\left(\frac{\partial p_{i,k}^{n+1}}{\partial\sigma}+\frac{\Delta\sigma}{2!}\frac{\partial^{2}p_{i,k}^{n+1}}{\partial\sigma^{2}}+O((\Delta\sigma)^{2})\right)\rightarrow-\frac{\sigma_{z}}{2\rho}\frac{\partial p_{i,k}^{n+1}}{\partial\sigma}$$

and finally

$$\left(\frac{\partial w}{\partial T}\right)^{n}=\frac{w_{i,k}^{n+1}-w_{i,k}^{*}}{\Delta T}+\frac{w_{i,k}^{*}-w_{i,k}^{n}}{\Delta T}=-\frac{\sigma_{z}}{2\rho}\frac{\partial p_{i,k}^{n+1}}{\partial\sigma}-\sigma_{t}\frac{\partial w_{i,k}^{n}}{\partial\sigma}-\frac{\sigma_{z}}{2\rho}\frac{\partial p_{i,k}^{n}}{\partial\sigma}$$

which shows the consistency of the numerical scheme for the vertical velocity equation.

Nomenclature

Latin:

a wave amplitude
d water depth
g gravity acceleration
h distance of the sea bed to the actual free surface
H wave height
k wave number ($2\pi/\lambda$)
p dynamic pressure caused by the acceleration of wave particles
t time
T wave period
u horizontal component of water particle's velocity
w vertical component of water particle's velocity
x horizontal coordinate in physical domain
X horizontal coordinate in computational domain
z vertical coordinate in physical domain

Greek:

ΔT time step length in computational domain
ΔX spatial step length on the horizontal axis in computational domain
$\Delta\sigma$ spatial step length on the vertical axis in computational domain
η free surface elevation vertically above the still water level
λ wavelength
ρ water density
σ horizontal coordinate in computational domain
ω wave angular frequency ($2\pi/T$)

Acronyms:

FD Finite difference
FE Finite element
FV Finite volume